

# BTI-Net: Bidirectional Decoder-Level Task Interaction via Uncertainty-Aware Gating for Multi-Task Medical Image Analysis

Abdullah Al Shafi<sup>1†</sup> Md Kawsar Mahmud Khan Zunayed<sup>1†</sup>  
Safin Ahmmed<sup>1</sup> Sk Imran Hossain<sup>1</sup> Engelbert Mephu Nguifo<sup>2</sup>

<sup>1</sup>Khulna University of Engineering & Technology, Bangladesh <sup>2</sup>University Clermont Auvergne, France

## Abstract

*Jointly learning to segment and classify medical images demands cross-task synergy, yet encoder-sharing architectures limit decoder reconstruction to task-private representations, permanently discarding the boundary cues and semantic priors each branch could supply to the other. This work introduces BTI-Net, which establishes bidirectional communication at every decoder level through two parallel pathways via Task Interaction Modules (TIM). Spatial boundary context is gated into the classification branch, while global semantic priors multiplicatively modulate the decoder, with refined features propagating progressively from coarse semantics to fine boundary detail across all four decoder resolutions. Since cross-task interaction is not equally reliable for every input, Uncertainty Proxy Attention (UPA) gates each TIM output per instance and per level using three signals that capture cross-task alignment, scene complexity, and prediction confidence, without external annotations or additional inference passes. Experiments on three medical benchmarks spanning ultrasound, dermoscopy, and brain MRI demonstrate consistent improvements in segmentation IoU and classification accuracy over both encoder-sharing and decoder-interaction baselines. Ablation confirms adaptive gating contributes +2.36 IoU over fixed bidirectional interaction, and classification accuracy improves by up to +2.26 points over the strongest multi-task baseline. UPA’s uncertainty proxies serve as reliable single-pass task-failure signals without the overhead of stochastic sampling. Code: [https://github.com/C-loud-Nine/BTI-Net\\_MTL](https://github.com/C-loud-Nine/BTI-Net_MTL)*

## 1. Introduction

MTL enables a single model to address multiple related tasks jointly, with the dominant approach coupling a shared encoder to independent decoder heads. While efficient, this design restricts all inter-task communication to a coarse bottleneck, after which the decoders diverge independently.

<sup>†</sup>Equal contribution.

Segmentation recovers precise boundaries that could disambiguate classification; classification accumulates global semantic context that could resolve ambiguous spatial regions. Both signals are lost once the decoders diverge, a gap that is especially consequential in medical imaging where datasets are small, pathology is heterogeneous, and complementary task signals carry real diagnostic value.

Recent decoder-interaction methods partially address this. MTI-Net [23] shows decoder-level interaction outperforms encoder-sharing, but propagates information in one direction with fixed per-sample blending. DenseMTL [15] adds bidirectionality but applies uniform blending regardless of scene complexity. In medical imaging, per-instance adaptability is not optional: the appropriate interaction strength varies fundamentally across pathology types, imaging conditions, and lesion morphology.

Addressing both limitations, BTI-Net introduces Task Interaction Modules (TIM) for bidirectional decoder-level communication, paired with Uncertainty Proxy Attention (UPA) for per-instance adaptive gating. TIM establishes bidirectional communication at every decoder level, from coarsest semantics to finest boundary detail: spatially aggregated boundary cues are injected into the classification vector through a gated residual (Seg→Clf), while global semantic priors are multiplicatively broadcast across the decoder map (Clf→Seg), with refined features carried forward progressively across all four resolutions. UPA gates each TIM output per instance and per level using three signals that capture cross-task alignment, scene complexity, and prediction confidence. Independent sigmoid weights allow both tasks to be simultaneously enhanced when interaction is reliable; on easy samples the gate remains conservative, preserving the unperturbed representations. A difficulty-aware loss aligns the gate with per-sample task performance, requiring no external annotations and no additional inference passes.

Evaluated on three publicly available benchmarks spanning ultrasound, dermoscopy, and brain MRI, BTI-Net advances both segmentation and classification consistently

across modalities. Ablation confirms that adaptive gating contributes +2.36 IoU over fixed bidirectional interaction, and the complete model improves classification accuracy by up to +2.26 points over the strongest multi-task baseline.

The main contributions are:

1. TIM: bidirectional decoder-level interaction between segmentation and classification via channel-wise gated operations, with refined spatial features propagated progressively across all four decoder resolutions.
2. UPA: a per-instance, per-level adaptive gate using three interpretable uncertainty signals, trained from per-sample difficulty scores derived automatically from task performance, without external annotations or Bayesian overhead.
3. Cross-modality validation on three diverse medical benchmarks, including, to the best of our knowledge, the first decoder-interaction MTL evaluation on BRISC.

## 2. Related Work

### 2.1. Multi-Task Learning Architectures

MTL architectures divide broadly into encoder-sharing and decoder-interaction approaches. Encoder-sharing methods [4, 8, 14] couple a common feature extractor to task-specific heads that diverge during upsampling, leaving cross-task signals untapped after the shared bottleneck.

Several works introduce cross-task connections during upsampling. PAD-Net [27] distills auxiliary task predictions into final tasks unidirectionally, establishing the pattern of using intermediate task outputs to guide final predictions. MTI-Net [23] models interactions at every backbone scale via distillation units, showing decoder-level interaction outperforms encoder-sharing; however, the flow is strictly unidirectional with identical blending applied to every sample. DenseMTL [15] adds bidirectional pairwise cross-task attention in decoder exchange blocks, yet applies a fixed blending weight regardless of scene complexity. Transformer-based methods such as InvPT [28] and TaskPrompter [29] model dependencies through global self-attention across task tokens; because they operate on joint token sets rather than explicit directed pathways, they do not provide the separate per-task gating that characterizes bidirectional decoder interaction.

Three limitations persist across all prior decoder-interaction methods: attention costs that grow with spatial resolution make them poorly suited to small medical datasets; fixed blending ignores per-instance variability in cross-task reliability; and none has been evaluated on medical imaging. BTI-Net addresses all three: TIM’s cost scales with channel dimension rather than spatial resolution, UPA provides per-instance adaptive gating, and the method is validated across three medical modalities, as summarized in Table 1.

Table 1. Positioning of BTI-Net against representative MTL architectures. *Decoder*: cross-task connections via explicit directed pathways; *Bidir.*: both tasks update each other at the same resolution; *Per-inst.*: interaction strength adapts per sample; *Medical*: validated on medical imaging.

Method	Decoder	Bidir.	Per-inst.	Medical
MTAN [14]	✗	✗	✗	✓
PAD-Net [27]	✓	✗	✗	✗
MTI-Net [23]	✓	✗	✗	✗
MTANet [13]	✗	✗	✗	✓
MTL-OCA [9]	✗	✗	✗	✓
DenseMTL [15]	✓	✓	✗	✗
InvPT [28]	✓	✗	✗	✗
DynaShare [18]	✗	✗	✓	✗
<b>BTI-Net</b>	✓	✓	✓	✓

### 2.2. Uncertainty in Multi-Task Learning

Uncertainty modelling in MTL has focused primarily on task-level loss balancing. Kendall et al. [12] proposed weighting losses by homoscedastic task uncertainty, while GradNorm [6] and PCGrad [30] balance tasks by normalising or projecting conflicting gradients. MTANet [13] and MTL-OCA [9] extend these ideas with attention-based dynamic weighting. All these approaches operate at the task level—scaling each task’s loss contribution—and cannot modulate cross-task feature exchange strength for individual inputs.

Monte Carlo dropout offers per-sample uncertainty estimates but requires multiple stochastic forward passes, prohibitive for dense prediction. The closest approach to instance-level feature adaptation is DynaShare [18], which learns a per-input gating policy over encoder layers; however, it gates layer execution rather than cross-task feature exchange, requires a separate policy network, and has not been applied to dense medical analysis. UPA gates cross-task enhancement per instance and per decoder level without additional inference cost.

### 2.3. Medical Image Analysis with MTL

Joint segmentation and classification has been widely studied for ultrasound [9, 13], dermoscopy [26], and brain MRI [16]. MTANet [13] and MTL-OCA [9] incorporate attention and optimal channel selection to improve task synergy; MFFMT [25] introduces adaptive multi-feature fusion to reduce information-sharing conflicts. All these methods operate within the encoder-sharing paradigm, apply fixed interaction strategies to every sample, and have been evaluated on a single modality, leaving cross-modal generalizability and decoder-level interaction in medical imaging as open problems.

### 3. Method

The proposed framework augments an EfficientNet-B4 [20] encoder with two modules, TIM and UPA, that together enable adaptive bidirectional task interaction at every decoder level. Figure 1 shows the complete pipeline. The encoder comprises five hierarchical stages ( $s_1$ : 144-ch,  $s_2$ : 192-ch,  $s_3$ : 336-ch,  $s_4$ : 960-ch, bridge: 1792-ch), each followed by a Multi-Scale Context Fusion (MSCF) block that applies three parallel dilated separable convolutions ( $r \in \{1, 2, 4\}$ ) with squeeze-and-excitation scale weighting [5, 10]. A four-level decoder ( $D_1$ – $D_4$ , channels 384/192/96/48, resolutions  $14^2$ – $112^2$ ) reconstructs the segmentation mask via transposed convolutions and attention-gated skip connections [17]. At every decoder level, TIM establishes bidirectional cross-task communication and UPA gates the resulting enhancement per instance before the output is upsampled to the next level. A  $224 \times 224$  segmentation head and a multi-scale classification head aggregating 4304-D of encoder and decoder features (Sec. 3.2) produce the dual-task predictions.

#### 3.1. Task Interaction Module

Prior decoder-interaction methods either propagate information unidirectionally or apply fixed per-sample blending; TIM addresses both by establishing *bidirectional* communication at *every* decoder level.

At level  $\ell \in \{1, 2, 3, 4\}$ , let  $D_\ell \in \mathbb{R}^{B \times H_\ell \times W_\ell \times C_\ell}$  denote the decoder feature map and  $f_{\text{clf}}^\ell \in \mathbb{R}^{B \times 256}$  a level-specific classification vector. Each  $f_{\text{clf}}^\ell$  is initialized by global average pooling (GAP) and a learned linear projection from the encoder stage whose semantic abstraction best matches that decoder level: bridge (1792-D)  $\rightarrow D_1$ ,  $s_4$  (960-D)  $\rightarrow D_2$ ,  $s_3$  (336-D)  $\rightarrow D_3$ ,  $s_2$  (192-D)  $\rightarrow D_4$ . This pairing anchors the most abstract representation at the coarsest decoder level and progressively finer spatial cues at deeper levels.

In the Seg $\rightarrow$ Clf direction, spatial boundary context recovered by the decoder is injected into the classification vector through a gated residual. A  $1 \times 1$  convolution reduces the decoder map to  $C_\ell/2$  channels before global average pooling yields a compact spatial summary  $\mathbf{z}_\ell$ , which is then projected and gated:

$$\mathbf{z}_\ell = \text{GAP}(\text{Conv}_{1 \times 1}^{C_\ell/2}(D_\ell)), \quad (1)$$

$$\mathbf{c}_\ell = \text{Dense}_{256}(\text{ReLU}(\mathbf{z}_\ell)), \quad (2)$$

$$\mathbf{g}_{\text{clf}} = \sigma(\text{Dense}_{256}(\mathbf{c}_\ell)), \quad (3)$$

$$f_{\text{clf}}^{\ell, \text{enh}} = f_{\text{clf}}^\ell + \mathbf{g}_{\text{clf}} \odot \mathbf{c}_\ell. \quad (4)$$

The element-wise gate  $\mathbf{g}_{\text{clf}} \in [0, 1]^{256}$  selects which spatial cues to admit per sample, while the residual in Eq. (4) preserves the original classification semantics.

In the complementary Clf $\rightarrow$ Seg direction, global semantic priors from the classification branch modulate the decoder feature map channel-wise. The classification vector is pro-

jected to the decoder’s channel space and combined with a self-gate derived from the decoder features:

$$\mathbf{u}_{\text{clf}} = \sigma(\text{Dense}_{C_\ell}(f_{\text{clf}}^\ell)) \in \mathbb{R}^{B \times 1 \times 1 \times C_\ell}, \quad (5)$$

$$\mathbf{g}_{\text{seg}} = \sigma(\text{Dense}_{C_\ell}(\text{GAP}(D_\ell))), \quad (6)$$

$$\boldsymbol{\mu}_\ell = \mathbf{1} + \tau \cdot \mathbf{g}_{\text{seg}} \odot \mathbf{u}_{\text{clf}}, \quad (7)$$

$$D_\ell^{\text{enh}} = D_\ell \odot \boldsymbol{\mu}_\ell. \quad (8)$$

The self-gate  $\mathbf{g}_{\text{seg}}$  adapts the modulation so that only channels already consistent with the semantic prior are amplified. The scalar  $\tau = 0.7$  bounds the multiplicative factor to  $[1, 1.7]$  and was selected by grid search over  $\tau \in \{0.3, 0.5, 0.7, 1.0\}$ .

Both pathways receive the *original* pre-interaction features as input, making them parallel operations that prevent double-counting: boundary context injected into the classifier does not contaminate the segmentation modulation. Each  $D_\ell^{\text{final}}$  (produced by UPA, Sec. 3.2) feeds the transposed convolution constructing  $D_{\ell+1}$ , so refinements accumulate from coarse semantic exchange at  $D_1$  ( $14 \times 14$ ) to fine boundary detail at  $D_4$  ( $112 \times 112$ ). The classification branch follows a complementary design: each level draws a fresh encoder-initialized vector and all four UPA-gated outputs are aggregated at the multi-scale head, fusing cross-task information from every decoder resolution without cross-level propagation of intermediate representations.

#### 3.2. Uncertainty Proxy Attention

Cross-task enhancement is not uniformly beneficial: on ambiguous low-contrast inputs, TIM-enhanced features may carry misleading signals, making reversion toward the original representations the safer choice. UPA interpolates between pre-TIM features ( $D_\ell, f_{\text{clf}}^\ell$ ) and TIM-enhanced features ( $D_\ell^{\text{enh}}, f_{\text{clf}}^{\ell, \text{enh}}$ ) using two independent scalar weights  $w_{\text{seg}}, w_{\text{clf}} \in [0, 1]$  per sample and per level, produced by a two-layer MLP driven by three uncertainty signals.

Three signals form the gate descriptor  $\mathbf{u}_\ell = [a_\ell, E_{\text{seg}}, E_{\text{clf}}] \in \mathbb{R}^3$ . The first, cross-task alignment  $a_\ell$ , measures whether TIM moves both branches in consistent latent directions; the spatially averaged TIM residuals are projected to a shared space and their cosine similarity computed:

$$a_\ell = \cos(\mathbf{p}_{\text{seg}}, \mathbf{p}_{\text{clf}}), \quad (9)$$

$$\mathbf{p}_{\text{seg}} = \mathbf{W}_s \text{GAP}(D_\ell^{\text{enh}} - D_\ell),$$

$$\mathbf{p}_{\text{clf}} = \mathbf{W}_c (f_{\text{clf}}^{\ell, \text{enh}} - f_{\text{clf}}^\ell).$$

The second, segmentation gradient energy  $E_{\text{seg}}$ , captures scene complexity via the mean absolute spatial gradient of the pre-TIM decoder map, where high values indicate

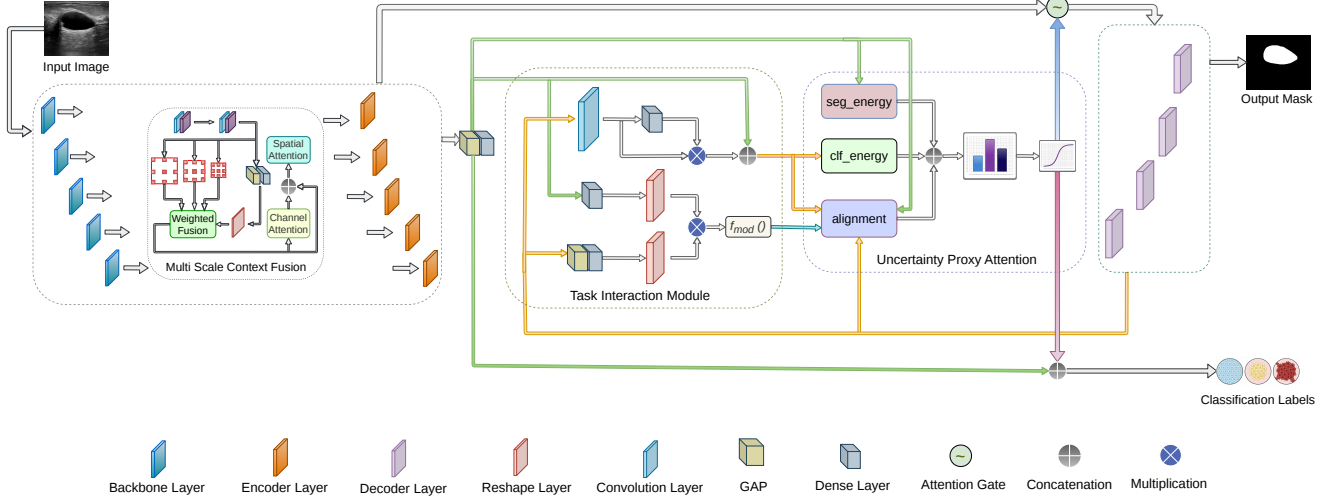


Figure 1. Architecture overview. Multi-scale context fusion augments encoder features at each stage. TIM establishes bidirectional task interaction at all four decoder levels. UPA gates the interaction strength per instance using three interpretable uncertainty proxies. Dual heads produce the segmentation mask and classification prediction.

intrinsically harder segmentation:

$$E_{\text{seg}} = \frac{1}{C_\ell H_\ell W_\ell} \sum_{c,i,j} (|D_\ell^{(i+1,j)} - D_\ell^{(i,j)}| + |D_\ell^{(i,j+1)} - D_\ell^{(i,j)}|). \quad (10)$$

The third, classification activation spread  $E_{\text{clf}}$ , distinguishes confident peaked distributions from flat uncertain ones through the log-variance of the enhanced classification vector:

$$E_{\text{clf}} = \log\left(1 + \frac{1}{256} \sum_{k=1}^{256} (f_{\text{clf}}^{\ell, \text{enh}}[k] - \bar{f}_{\text{clf}}^{\ell, \text{enh}})^2\right). \quad (11)$$

Together,  $a_\ell$ ,  $E_{\text{seg}}$ , and  $E_{\text{clf}}$  span interaction coherence, scene complexity, and prediction confidence, covering three complementary uncertainty axes without additional inference passes or external annotations.

The descriptor  $\mathbf{u}_\ell$  is mapped by a two-layer MLP to two logits, and sigmoid activation yields independent gate weights:

$$[w_{\text{seg}}, w_{\text{clf}}] = \sigma(\text{Dense}_2(\text{ReLU}(\text{Dense}_{32}(\mathbf{u}_\ell)))). \quad (12)$$

Sigmoid is used rather than softmax because the zero-sum constraint  $w_{\text{seg}} + w_{\text{clf}} = 1$  suppresses one task whenever the other is enhanced, even on easy samples where both branches are reliable. Independent sigmoid weights allow both to approach 1 simultaneously, making UPA a confidence-based interpolator rather than a task selector. The final features are produced by residual interpolation:

$$D_\ell^{\text{final}} = D_\ell + w_{\text{seg}} (D_\ell^{\text{enh}} - D_\ell), \quad (13)$$

$$f_{\text{clf}}^{\ell, \text{final}} = f_{\text{clf}}^\ell + w_{\text{clf}} (f_{\text{clf}}^{\ell, \text{enh}} - f_{\text{clf}}^\ell). \quad (14)$$

A difficulty-aware auxiliary loss trains  $w_{\text{seg}}$  and  $w_{\text{clf}}$  directly on per-sample task performance without external annotations. Per-sample soft-IoU values are min-max normalized within the mini-batch and inverted so that the hardest sample receives a target of 1, encouraging the gate to be sensitive to sample difficulty:

$$t_i^{\text{seg}} = 1 - \frac{\text{IoU}_i - \text{IoU}_{\min}}{\text{IoU}_{\max} - \text{IoU}_{\min} + \epsilon}. \quad (15)$$

On ambiguous inputs where cross-task alignment  $a_\ell$  is low, the gate simultaneously receives a signal to suppress the interaction; the difficulty target and the alignment signal thus act complementarily, with the net realized enhancement reflecting both. An analogous target  $t_i^{\text{clf}}$  is derived from inverted min-max prediction confidence. The gate is trained by minimizing BCE between each target and its gate weight, averaged over all four UPA levels as  $\mathcal{L}_{\text{gate}}$ , yielding the complete training objective:

$$\mathcal{L} = \mathcal{L}_{\text{seg}} + \mathcal{L}_{\text{clf}} + \mathcal{L}_{\text{gate}}. \quad (16)$$

In practice,  $\mathcal{L}_{\text{gate}}$  is activated only in Stage 2 after the main network has converged; during Stage 1,  $\lambda_{\text{gate}} = 0$  and the model trains under  $\mathcal{L}_{\text{seg}} + \mathcal{L}_{\text{clf}}$  only.

After all four UPA levels, the classification branch aggregates the encoder's multi-scale features by global average pooling of  $s_2$ ,  $s_3$ ,  $s_4$ , and bridge (3280-D total), concatenated with the four 256-D  $f_{\text{clf}}^{\ell, \text{final}}$  vectors, yielding a 4304-D representation that fuses hierarchical encoder semantics with task-refined features across every decoder resolution.

## 4. Experiments and Results

### 4.1. Datasets and Implementation

Three publicly available benchmarks spanning distinct imaging modalities are used for evaluation. BUSI [2] comprises 780 breast ultrasound images across three clinical classes from 600 patients; normal cases carry empty segmentation masks and are excluded from IoU computation but retained for classification. HAM10000 [21] is a 10,015-image dermoscopic collection spanning seven diagnostic categories of pigmented skin lesions; the full dataset with expert-verified segmentation masks provided by Tschandl et al. [22] is used. BRISC [7] is a recently released brain MRI benchmark of 6,000 T1-weighted scans annotated with tumor segmentation masks and four-class tumor-type labels; splits are patient-wise with stratification across classes. Results are reported as mean and standard deviation over three independent seeds.

All models share an EfficientNet-B4 encoder pre-trained on ImageNet. Standard augmentation is applied during training. Segmentation uses Focal Tversky loss [1] ( $\gamma = 0.75$ ) and classification uses Focal Cross-Entropy ( $\gamma = 2.0$ ). Training proceeds in two stages: Stage 1 optimizes the full network under  $\mathcal{L}_{\text{seg}}$  and  $\mathcal{L}_{\text{clf}}$ ; Stage 2 freezes all parameters except the four UPA gate networks and introduces  $\mathcal{L}_{\text{gate}}$ , ensuring the gate is supervised by a stable predictor. Gate difficulty targets are derived from per-sample soft-IoU and prediction confidence, min-max normalized within the mini-batch; min-max is preferred over rank normalization because it preserves the magnitude of performance gaps, producing more discriminative gate supervision. The gate loss is applied with a stop-gradient on the task predictions, preventing the gate from gaming the soft-IoU score. IoU is computed over foreground lesion pixels only; Dice scores are provided in the supplementary material. All baselines are reproduced under identical conditions; full hyperparameter settings and additional uncertainty analyses are provided in the supplementary material. Single-task segmentation baselines are evaluated without a classification head.

### 4.2. Ablation Study

All ablations use BUSI under the protocol of Sec. 4.1 unless noted; uncertainty proxy evaluations extend to HAM10000 and BRISC to verify that observed proxy behavior is not modality-specific.

Figure 2 decomposes TIM’s feature modifications  $|\Delta f_{\text{clf}}|$  and  $|\Delta F_{\text{seg}}|$  by decoder level and sample difficulty (top vs. bottom IoU quartile). In the Seg→Clf direction, easy samples receive consistently larger enhancement than hard samples across all levels, peaking at  $D_2$ , consistent with globally coherent cases benefiting more from semantic-level cross-task agreement. In the Clf→Seg direction, both groups grow monotonically from  $D_1$  to  $D_4$ , but easy samples receive greater enhancement at every level and the gap widens at  $D_4$ ,

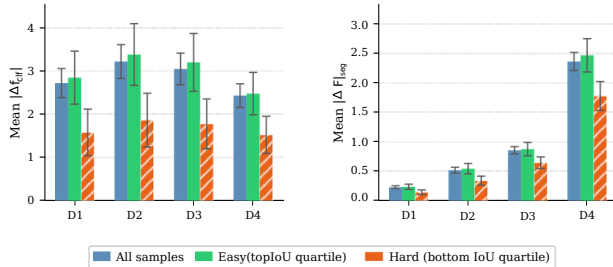


Figure 2. TIM feature shift magnitudes on BUSI by sample difficulty (top/bottom IoU quartile). *Left* (Seg→Clf): easy samples receive consistently larger enhancement, peaking at  $D_2$ . *Right* (Clf→Seg): both groups grow toward  $D_4$ , with easy samples maintaining larger absolute enhancement throughout.

Table 2. Segmentation-failure detection: AUC-ROC and AUPRC of  $w_{\text{seg}}$  vs. 30-pass MC Dropout. **Bold**: beats MC Dropout at that level.

Dataset	MC (30×)		D1		D2		D3		D4	
	AUC	PR	AUC	PR	AUC	PR	AUC	PR	AUC	PR
BUSI	0.751	0.431	<b>0.767</b>	<b>0.512</b>	<b>0.824</b>	<b>0.602</b>	0.682	0.333	<b>0.785</b>	<b>0.624</b>
BRISC	0.702	0.238	0.282	0.081	0.482	<b>0.247</b>	<b>0.834</b>	<b>0.412</b>	0.518	0.141
HAM	0.891	0.151	<b>0.901</b>	0.056	<b>0.918</b>	0.068	<b>0.934</b>	0.079	<b>0.926</b>	0.104

suggesting that boundary-clear inputs exploit class priors more effectively at fine resolutions while ambiguous hard samples remain gating-suppressed. This level-dependent allocation motivates a per-instance, per-level gate rather than a fixed dataset-wide blending coefficient.

UPA’s gate signals are evaluated as deterministic, single-pass failure proxies against 30-pass Monte Carlo Dropout. A sample is labelled a segmentation failure if  $\text{IoU} < 0.5$  and a classification failure if the predicted class is incorrect; these labels score the already-computed gate values and are never used to select or tune them. Table 2 reports AUC-ROC and AUPRC for  $w_{\text{seg}}$  at every decoder level without any level selection. On HAM10000,  $w_{\text{seg}}$  exceeds MC Dropout on AUC-ROC at all four levels; AUPRC remains below the MC reference, reflecting the near-zero segmentation failure rate (1.0%) that limits precision-recall discriminability. On BRISC the signal is informative mainly at  $D_3$ , consistent with the level-dependent enhancement patterns. The per-modality variation confirms that UPA’s reliability signal is level and modality-dependent rather than a single uniformly dominant proxy.

Table 3 compares MC Dropout, the parameter-free maximum-softmax-confidence baseline ( $1 - \text{conf}$ ), and the most discriminative UPA signal per dataset. AUPRC is the more informative metric at low failure rates and is reported alongside AUC-ROC. UPA surpasses MC Dropout on AUPRC across all three datasets. On BUSI,  $w_{\text{clf}}$  at

Table 3. Classification-failure detection: AUC-ROC and AUPRC. UPA exceeds MC Dropout on AUPRC across all three datasets. 1-conf achieves higher AUPRC on BRISC and HAM where softmax confidence is well-calibrated; UPA exceeds 1-conf on both AUC-ROC and AUPRC for BUSI.

Dataset	MC (30×)		1-conf		Best UPA Signal		
	AUC	PR	AUC	PR	Signal	AUC	PR
BUSI	0.728	0.264	0.834	0.529	$w_{\text{clf}}$ ( $D_4$ )	<b>0.850</b>	<b>0.543</b>
BRISC	0.397	0.013	<b>0.920</b>	<b>0.359</b>	$-\delta$ ( $D_1$ )	0.753	0.098
HAM	0.575	0.324	<b>0.834</b>	<b>0.561</b>	$w_{\text{clf}}$ ( $D_1$ )	0.766	0.394

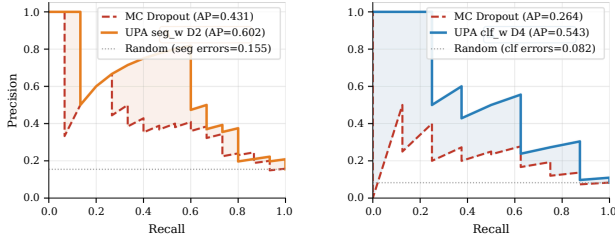


Figure 3. Precision-recall curves for failure detection on BUSI. UPA achieves  $AP = 0.602$  for segmentation ( $w_{\text{seg}}, D_2$ ) and  $AP = 0.543$  for classification ( $w_{\text{clf}}, D_4$ ), against MC Dropout baselines of 0.431 and 0.264.

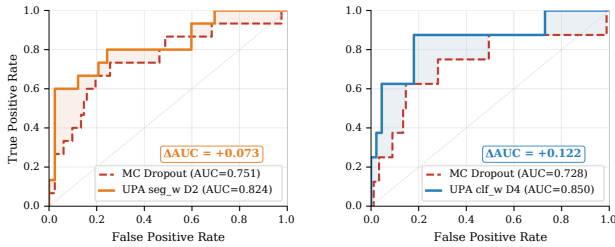


Figure 4. ROC curves for failure detection on BUSI across decoder levels  $D_1$ – $D_4$ .  $\Delta AUC = +0.073$  for segmentation ( $D_2$ ) and  $+0.122$  for classification ( $D_4$ ) over MC Dropout.

$D_4$  achieves 0.850 AUC, exceeding both MC Dropout (0.728) and the confidence baseline (0.834). On BRISC and HAM10000 the confidence baseline remains stronger (0.920 and 0.834); UPA trails it (0.753 and 0.766) while still exceeding MC Dropout, whose BRISC AUC (0.397) falls below chance due to a known dropout failure mode under class imbalance. Classification failure detection is not the primary claim; the result positions UPA’s gate as a useful secondary signal with no additional inference cost.

Figure 3 shows precision-recall curves on BUSI:  $w_{\text{seg}}$  at  $D_2$  achieves  $AP = 0.602$  against MC Dropout’s 0.431, and  $w_{\text{clf}}$  at  $D_4$  achieves  $AP = 0.543$  against 0.264. Figure 4 shows the corresponding ROC curves:  $w_{\text{seg}}$  at  $D_2$  improves AUC by  $+0.073$  over MC Dropout for segmentation, and  $w_{\text{clf}}$  at  $D_4$  improves by  $+0.122$  for classification.

Table 4. Component ablation on BUSI. Mean  $\pm$  std over three seeds.

Components			Results	
MSCF	TIM	UPA	Seg. IoU	Clf. Acc
✗	✗	✗	$67.43 \pm 1.21$	$84.62 \pm 1.08$
✓	✗	✗	$69.95 \pm 1.04$	$88.89 \pm 0.83$
✗	✓	✗	$69.20 \pm 1.13$	$86.32 \pm 0.94$
✓	✓	✗	$72.14 \pm 0.72$	$90.84 \pm 0.58$
✗	✓	✓	$70.48 \pm 0.91$	$91.47 \pm 0.62$
✓	✓	✓	<b><math>74.50 \pm 0.30</math></b>	<b><math>93.16 \pm 0.80</math></b>

Table 4 isolates each architectural component. MSCF alone provides  $+2.52$  IoU through multi-granularity encoder context. TIM alone yields  $+1.77$  IoU; its modest isolated gain reflects that cross-task interaction requires sufficiently rich encoder representations; paired with MSCF (row 4), the combined gain grows to  $+4.71$  IoU, confirming that multi-scale feature quality amplifies bidirectional interaction rather than the contributions being independent. Adding UPA to MSCF+TIM yields the full  $+7.07$  IoU, with UPA’s isolated contribution of  $+1.28$  growing to  $+2.36$  in the complete context, consistent with richer features providing more informative gate signals. The classification accuracy trajectory (row 4 vs. row 5) further reveals that UPA specifically benefits classification—TIM+UPA achieves higher Acc than MSCF+TIM despite lower IoU, because UPA adaptively suppresses low-confidence segmentation priors from contaminating the classification branch.

Replacing the independent sigmoid gates (Eq. (12)) with a softmax constraint creates a zero-sum constraint that penalizes easy samples where both tasks should be enhanced simultaneously. Removing the difficulty-aware gate regularization (Eq. (16)) drops a further  $-0.53$  IoU, indicating that direct supervision toward observed sample difficulty is necessary for the gate to learn a meaningful difficulty ranking rather than deferring entirely to the task losses.

### 4.3. Comparison with Prior Work

Comparisons are structured across two complementary tables. Table 6 evaluates segmentation performance under the most favorable conditions for each method: pure single-task segmentation training for architectures without a native multi-task design, and joint training for dedicated MTL methods. Table 5 restricts to methods that produce both outputs simultaneously.

Table 6 shows that BTI-Net achieves the highest segmentation IoU on all three benchmarks. On BUSI and BRISC, margins over MISSFormer are  $+1.86$  and  $+1.91$ , reflecting moderate benefit from cross-task boundary priors on ultrasound and brain MRI. On HAM10000 the gain is  $+2.98$ , consistent across both tables: the seven-class dermatology labels encode lesion-type priors that are uniquely informa-

Table 5. Joint segmentation and classification results (mean  $\pm$  std over three random seeds) for methods that produce both outputs simultaneously. **Bold**: best per metric–dataset pair.

Method	Year	BUSI		HAM10000		BRISC	
		IoU $\uparrow$	Acc $\uparrow$	IoU $\uparrow$	Acc $\uparrow$	IoU $\uparrow$	Acc $\uparrow$
MTAN [14]	2019	68.41 $\pm$ 1.12	87.84 $\pm$ 0.89	87.24 $\pm$ 0.84	85.73 $\pm$ 0.79	68.84 $\pm$ 0.87	93.42 $\pm$ 0.67
MTANet [13]	2024	71.24 $\pm$ 0.74	90.47 $\pm$ 0.63	87.12 $\pm$ 0.63	86.41 $\pm$ 0.64	71.84 $\pm$ 0.67	95.84 $\pm$ 0.52
MTL-OCA [9]	2025	72.14 $\pm$ 0.61	91.23 $\pm$ 0.49	86.84 $\pm$ 0.68	86.88 $\pm$ 0.52	71.24 $\pm$ 0.58	96.21 $\pm$ 0.36
MTI-Net [23]	2020	73.06 $\pm$ 0.55	90.84 $\pm$ 0.53	87.84 $\pm$ 0.44	86.73 $\pm$ 0.49	73.84 $\pm$ 0.46	95.96 $\pm$ 0.37
DenseMTL [15]	2023	72.83 $\pm$ 0.58	91.47 $\pm$ 0.51	88.14 $\pm$ 0.53	87.12 $\pm$ 0.43	74.61 $\pm$ 0.47	96.84 $\pm$ 0.32
<b>BTI-Net (Ours)</b>	2026	<b>74.50 <math>\pm</math> 0.30</b>	<b>93.16 <math>\pm</math> 0.80</b>	<b>89.80 <math>\pm</math> 0.20</b>	<b>87.84 <math>\pm</math> 0.58</b>	<b>76.74 <math>\pm</math> 0.52</b>	<b>99.10 <math>\pm</math> 0.20</b>

Table 6. Segmentation IoU (mean  $\pm$  std over three random seeds). †: evaluated in single-task segmentation mode. **Bold**: best per dataset.

Method	Year	BUSI	HAM10000	BRISC
<i>CNN-based segmentation</i>				
U-Net [19]†	2015	66.42 $\pm$ 1.12	80.12 $\pm$ 0.94	65.84 $\pm$ 0.87
Att-U-Net [17]†	2018	67.89 $\pm$ 0.89	81.84 $\pm$ 0.83	68.12 $\pm$ 0.79
UNet++ [31]†	2020	69.12 $\pm$ 0.96	84.73 $\pm$ 0.84	71.84 $\pm$ 0.81
<i>Transformer-based segmentation</i>				
TransUNet [24]†	2024	70.51 $\pm$ 0.71	83.84 $\pm$ 0.68	71.28 $\pm$ 0.74
Swin-UNet [3]†	2022	71.24 $\pm$ 0.63	85.14 $\pm$ 0.46	73.42 $\pm$ 0.52
MISSFormer [11]†	2023	72.64 $\pm$ 0.54	86.82 $\pm$ 0.49	74.83 $\pm$ 0.51
<b>BTI-Net (Ours)</b>	2026	<b>74.50 <math>\pm</math> 0.30</b>	<b>89.80 <math>\pm</math> 0.20</b>	<b>76.74 <math>\pm</math> 0.52</b>

tive for spatial boundary discrimination between morphologically similar lesion categories—priors that single-task models cannot access regardless of architectural capacity.

Table 5 reports joint performance across all six metric–dataset pairs, with BTI-Net leading on each. The progression within the MTL group is architecturally coherent but not uniform, and reveals dataset-dependent behavior that is informative in its own right. On BUSI and BRISC, encoder-sharing methods underperform single-task transformers on segmentation IoU, confirming that the encoder-sharing penalty outweighs task-label benefits when data are limited or domain mismatch is present. On HAM10000, MTAN approaches and slightly exceeds MISSFormer’s single-task segmentation IoU (+0.42), reflecting the partial compensation that rich seven-class labels provide to shared encoder representations when training data are abundant; yet MTAN’s classification accuracy on HAM10000 remains the weakest among all MTL methods, indicating that the segmentation benefit does not transfer symmetrically to the classification branch. This asymmetry also produces a crossover: MTANet outperforms MTAN on BUSI (where medical-specific ultrasound attention dominates) but falls behind MTAN on HAM10000 (where data volume and label richness favor general encoder sharing). Decoder-interaction methods (MTI-Net, DenseMTL) exceed single-task transformers across all three

datasets, confirming that injecting classification priors during spatial reconstruction is the dominant driver of improvement; a second crossover appears here, with DenseMTL trailing MTI-Net on small BUSI ( $-0.23$  IoU) but surpassing it on HAM10000 and BRISC, where the larger datasets support the richer pairwise cross-task attention. BTI-Net extends this further: against MTI-Net, segmentation IoU improves by +1.44, +1.96, and +2.90 on BUSI, HAM10000, and BRISC, while against DenseMTL the gains are +1.67, +1.66, and +2.13, attributable to per-instance adaptive gating over fixed bidirectional blending. On BRISC, BTI-Net reaches 99.10% classification accuracy (+2.26 over DenseMTL), demonstrating that decoder-level cross-task gating extracts strong discriminative signals for the four-class brain tumor task even when segmentation margins are narrower.

Figure 5 presents representative segmentation outputs across all three modalities. BTI-Net recovers sharper lesion boundaries with fewer false positives, particularly in low-contrast regions where encoder-sharing methods produce over-segmented blobs. Against MTI-Net and DenseMTL, the improvement is most visible at object boundaries: the Clf→Seg pathway injects class-specific priors that suppress activations inconsistent with the predicted lesion type, an effect absent in methods that apply fixed per-sample blending. Failure cases are provided in the supplementary material.

## 5. Conclusion

BTI-Net addresses a recognized gap in multi-task medical image analysis: the absence of cross-task refinement during spatial reconstruction. Task Interaction Modules establish bidirectional decoder-level communication at all four resolutions, creating a progressive closed loop from coarse semantic exchange at  $D_1$  to fine boundary correction at  $D_4$ . Uncertainty Proxy Attention gates each interaction per instance and per level using three signals derived from feature activation statistics, without external annotations or Bayesian overhead.

Evaluation across three diverse imaging modalities (breast ultrasound, dermoscopy, and brain MRI) over three independent seeds demonstrates consistent improvement

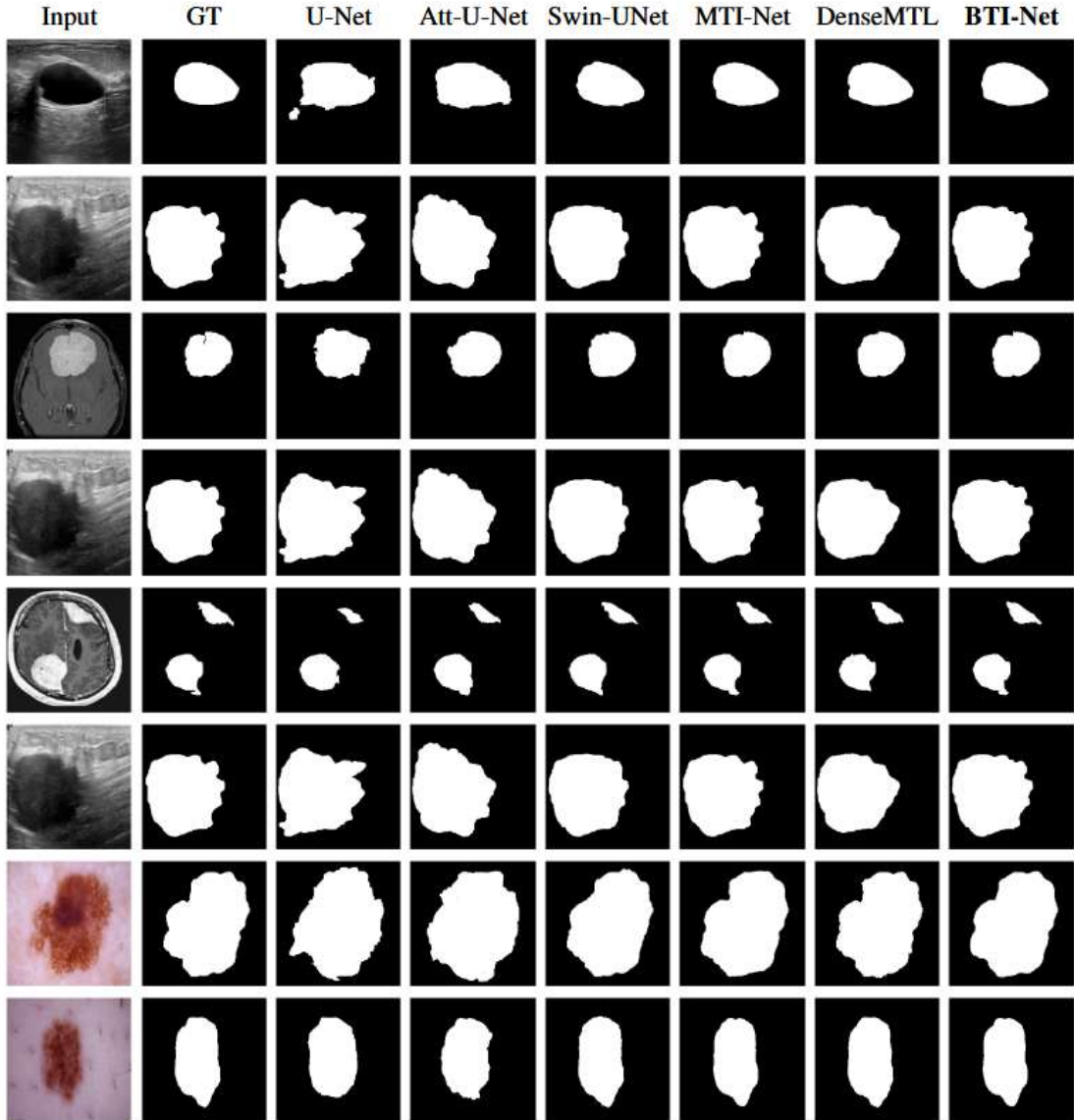


Figure 5. Qualitative segmentation results. **Rows 1–2:** BUSI (ultrasound); **Rows 3–4:** BRISC (brain MRI); **Rows 5–8:** HAM10000 (dermoscopy). **Columns:** input, ground truth, U-Net, Att-U-Net, Swin-UNet, MTI-Net, DenseMTL, BTI-Net. Cases are selected to highlight boundary-ambiguous examples where bidirectional cross-task interaction provides the clearest visual improvement.

over both encoder-sharing methods and prior decoder-interaction approaches including MTI-Net and DenseMTL across all six metric–dataset pairs. Ablation confirms that adaptive gating contributes +2.36 IoU over fixed bidirectional interaction, and that difficulty-aware supervision is necessary for the gate to learn a meaningful difficulty ranking.

UPA provides competitive single-pass failure signals, matching or exceeding MC Dropout on segmentation AUC-ROC across all benchmarks; classification failure detection surpasses MC Dropout in AUPRC across all three

datasets, though UPA does not uniformly close the gap to the maximum-softmax-confidence baseline, pointing toward task-specific uncertainty heads as a direction for future work.

The framework is compatible with standard encoder backbones and applicable to other multi-task dense prediction settings with complementary inter-task structure. Extending the design to 3D volumetric data and to natural-image task pairs such as semantic segmentation with depth estimation are natural next steps.

## References

- [1] Nabila Abraham and Naimul Mefraz Khan. A novel focal Tversky loss function with improved attention U-Net for lesion segmentation. In *ISBI*, pages 683–687, 2019. 5
- [2] Walid Al-Dhabyani, Mohammed Gomaa, Hussien Khaled, and Aly Fahmy. Dataset of breast ultrasound images. *Data in Brief*, 28:104863, 2020. 5
- [3] Hu Cao et al. Swin-UNet: Unet-like pure transformer for medical image segmentation. In *ECCV Workshops*, pages 205–218, 2022. 7
- [4] Rich Caruana. Multitask learning. *Machine Learning*, 28(1): 41–75, 1997. 2
- [5] Liang-Chieh Chen, George Papandreou, Iasonas Kokkinos, Kevin Murphy, and Alan L. Yuille. DeepLab: Semantic image segmentation with deep convolutional nets, atrous convolution, and fully connected CRFs. *IEEE Transactions on Pattern Analysis and Machine Intelligence*, 40(4):834–848, 2018. 3
- [6] Zhao Chen, Vijay Badrinarayanan, Chen-Yu Lee, and Andrew Rabinovich. GradNorm: Gradient normalization for adaptive loss balancing in deep multitask networks. In *ICML*, pages 794–803, 2018. 2
- [7] A. Fateh, Y. Rezvani, S. Moayedi, et al. BRISC: Annotated dataset for brain tumor segmentation and classification. *Scientific Data*, 13:361, 2026. 5
- [8] Yuan Gao et al. MTL-NAS: Task-agnostic neural architecture search for multi-task learning. In *ECCV*, pages 512–527, 2020. 2
- [9] Yuan Gao et al. Multi-task learning with optimal channel attention for breast ultrasound diagnosis. *Frontiers in Oncology*, 15:1567577, 2025. 2, 7
- [10] Jie Hu, Li Shen, and Gang Sun. Squeeze-and-excitation networks. In *CVPR*, pages 7132–7141, 2018. 3
- [11] Xiaoming Huang, Zhifang Deng, Dandan Li, and Xueguang Yuan. MISSFormer: An effective medical image segmentation transformer. *IEEE Transactions on Medical Imaging*, 42(5):1573–1586, 2023. 7
- [12] Alex Kendall, Yarin Gal, and Roberto Cipolla. Multi-task learning using uncertainty to weigh losses. In *CVPR*, pages 7482–7491, 2018. 2
- [13] Y. Ling, Y. Wang, W. Dai, J. Yu, P. Liang, and D. Kong. MTANet: Multi-task attention network for automatic medical image segmentation and classification. *IEEE Transactions on Medical Imaging*, 43(2):674–685, 2024. 2, 7
- [14] Shikun Liu, Edward Johns, and Andrew J. Davison. End-to-end multi-task learning with attention. In *CVPR*, pages 1871–1880, 2019. 2, 7
- [15] Ivan Lopes, Tuan-Hung Vu, and Raoul de Charette. Cross-task attention mechanism for dense multi-task learning. In *WACV*, pages 2674–2683, 2023. 1, 2, 7
- [16] Andriy Myronenko. 3D MRI brain tumor segmentation using autoencoder regularization. In *BrainLes, MICCAI*, pages 311–320, 2019. 2
- [17] Ozan Oktay et al. Attention U-Net: Learning where to look for the pancreas. In *MIDL*, 2018. 3, 7
- [18] Ehsan Rahimian, Golar Javadi, Frederick Tung, and Gabriela Oliveira. DynaShare: Task and instance conditioned parameter sharing for multi-task learning. In *CVPR Workshops*, pages 4535–4543, 2023. 2
- [19] Olaf Ronneberger, Philipp Fischer, and Thomas Brox. U-Net: Convolutional networks for biomedical image segmentation. In *MICCAI*, pages 234–241, 2015. 7
- [20] Mingxing Tan and Quoc V. Le. EfficientNet: Rethinking model scaling for convolutional neural networks. In *ICML*, pages 6105–6114, 2019. 3
- [21] Philipp Tschandl, Cliff Rosendahl, and Harald Kittler. The HAM10000 dataset, a large collection of multi-source dermatoscopic images of common pigmented skin lesions. *Scientific Data*, 5:180161, 2018. 5
- [22] Philipp Tschandl, Christoph Rinner, Zoe Apalla, et al. Human-computer collaboration for skin cancer recognition. *Nature Medicine*, 26:1229–1234, 2020. 5
- [23] Simon Vandenhende, Stamatios Georgoulis, and Luc Van Gool. MTI-Net: Multi-scale task interaction networks for multi-task learning. In *ECCV*, pages 527–543, 2020. 1, 2, 7
- [24] Lin Wang et al. TransUNet: Advanced transformer-based architectures for medical image segmentation. *IEEE Transactions on Medical Imaging*, 2024. Early access. 7
- [25] Jianwei Wei et al. A novel deep learning model for breast tumor ultrasound image classification with lesion region perception. *Current Oncology*, 31(9):5552–5572, 2024. 2
- [26] Yutong Xie, Jianpeng Zhang, Yong Xia, and Chunhua Shen. A mutual bootstrapping model for automated skin lesion segmentation and classification. *IEEE Transactions on Medical Imaging*, 39(7):2482–2493, 2020. 2
- [27] Dan Xu, Wanli Ouyang, Xiaogang Wang, and Nicu Sebe. PAD-Net: Multi-tasks guided prediction-and-distillation network. In *CVPR*, pages 675–684, 2018. 2
- [28] Hanrong Ye and Dan Xu. Inverted pyramid multi-task transformer for dense scene understanding. In *ECCV*, pages 514–530, 2022. 2
- [29] Hanrong Ye and Dan Xu. TaskPrompter: Spatial-channel multi-task prompting for dense scene understanding. In *ICLR*, 2023. 2
- [30] Tianhe Yu et al. Gradient surgery for multi-task learning. In *NeurIPS*, 2020. 2
- [31] Zongwei Zhou et al. UNet++: A nested U-Net architecture. In *DLMIA, MICCAI*, pages 3–11, 2018. 7

# BTI-Net: Bidirectional Decoder-Level Task Interaction via Uncertainty-Aware Gating for Multi-Task Medical Image Analysis

## Supplementary Material

---

### A. Theoretical Motivation for UPA Signals

The three signals used by UPA, cross-task alignment, segmentation gradient energy, and classification activation spread, proxy distinct sources of predictive uncertainty without requiring multiple stochastic forward passes. Each signal is justified below in terms of its relationship to model confidence and expected error probability.

**Cross-task alignment as epistemic uncertainty.** When TIM produces feature updates, the residuals  $\Delta_{\text{seg}} = D_{\ell}^{\text{enh}} - D_{\ell}$  and  $\Delta_{\text{clf}} = f_{\text{clf}}^{\ell, \text{enh}} - f_{\text{clf}}^{\ell}$  encode how each task’s representation is modified by the interaction. If both residuals point in similar directions after projection, the interaction is *mutually consistent*. Conversely, low cosine similarity signals *epistemic uncertainty*: the two branches disagree on how to incorporate cross-task information, indicating the interaction is unreliable for this sample. Formally,  $a_{\ell}$  is a sample-wise estimate of directional agreement between the two task update vectors.

**Segmentation gradient energy as aleatoric complexity.**  $E_{\text{seg}}$  measures the mean absolute first-order spatial differences of the base decoder features. Sharp boundaries, fine structures, and heterogeneous textures produce large local gradients, representing *aleatoric uncertainty* inherent to the input. This signal naturally increases at finer decoder resolutions ( $D_3, D_4$ ) where boundary detail is most pronounced, making it scale-appropriate without requiring separate scale-specific signals.

**Classification activation spread as prediction confidence.**  $E_{\text{clf}}$  captures how peaked the classification feature vector is via its log-variance. A high value indicates a low-entropy prediction concentrated on dominant channels; a low value indicates a flat, uninformative embedding. This serves as a proxy for *classification confidence*, related to the softmax margin and expected calibration error. Extracting spread from pre-softmax features rather than class probabilities makes it sensitive to the network’s internal representation even when final probabilities are poorly calibrated.

**Completeness.** Together,  $a_{\ell}$ ,  $E_{\text{seg}}$ , and  $E_{\text{clf}}$  span three complementary axes: interaction consistency, scene complexity, and prediction confidence. These axes are non-

redundant: a low-contrast image may have low gradient energy but low classification confidence; a texture-rich image may have high gradient energy but high inter-task alignment. No single signal covers all three axes.

### B. Training Protocol Details

**Two-stage training.** Training proceeds in two stages to ensure the UPA gate learns from a stable main network rather than a randomly initialized predictor.

Stage 1 trains the full model end-to-end: encoder, decoder, TIM modules, UPA modules, and both heads under the objective  $\mathcal{L} = \mathcal{L}_{\text{seg}} + \mathcal{L}_{\text{clf}}$  with all parameters trainable. Stage 1 runs for up to 50 epochs with early stopping on validation IoU (patience 10).

Stage 2 freezes all layers *except* the four UPA gate networks and fine-tunes only the gate parameters on  $\mathcal{L}_{\text{gate}}$ , isolating UPA convergence from changes in the backbone and TIM. Stage 2 runs for up to 15 epochs with early stopping (patience 5).

**Learning rate schedule.** Both stages use an initial learning rate of  $3 \times 10^{-4}$ , reduced on validation plateau by a factor of 0.5 every 5 epochs without improvement (minimum  $10^{-6}$ ). Gradient norms are clipped at 1.0 to prevent instability during early training.

**Loss weight adaptation.** An adaptive scheme initialises task weights at  $\lambda_{\text{seg}} = 0.82$ ,  $\lambda_{\text{clf}} = 0.18$  and adjusts them proportionally based on relative validation loss improvement at each epoch. The gate regularisation weight  $\lambda_{\text{gate}}$  is set to 1.0 for HAM10000 and BRISC, and 0.5 for BUSI; the lower value on BUSI reflects the smaller dataset size and higher noise in soft-IoU estimates.

**Data splits.** BUSI and HAM10000 are split into approximately 70/15/15 train/validation/test partitions with stratified label distributions; BRISC follows the official test split, with the remaining training data split 85/15 for training/validation. Three independent random seeds (42, 123, 456) are used; each seed determines parameter initialization and augmentation order

## C. Hyperparameter Settings

Table A1. Hyperparameter settings used across experiments. Values are consistent across all three datasets unless explicitly noted.

Parameter	Value
<i>Optimisation &amp; Training</i>	
Optimizer	Adam
Initial learning rate	$3 \times 10^{-4}$
Learning rate schedule	ReduceLROnPlateau (factor 0.5, patience 5)
Weight decay ( $L_2$ )	$10^{-5}$
Max epochs (Stage 1 & 2)	50 / 15
Early stopping patience	10 (val IoU) / 5 (val loss)
Batch size (Train / Val)	8 / 16
<i>Architecture</i>	
Encoder backbone	EfficientNet-B4 (ImageNet pre-trained)
Decoder channels	384, 192, 96, 48
Classification feature dim	256-D (per level)
UPA (hidden / projection dim)	32 / 64
Dropout rate	0.3 (classification head)
<i>Loss Functions &amp; Balancing</i>	
Segmentation loss	Focal Tversky ( $\gamma = 0.75$ )
Classification loss	Focal Cross-Entropy ( $\gamma = 2.0$ )
Initial task weights	$\lambda_{\text{seg}} = 0.82, \lambda_{\text{clf}} = 0.18$ (adaptive)
Auxiliary loss weights	Boundary (0.25), Texture (0.15)
Gate weight $\lambda_{\text{gate}}$	0.5 (BUSI); 1.0 (HAM, BRISC)
TIM modulation $\tau$	0.7
<i>Data Configuration</i>	
Input resolution	$224 \times 224$
Augmentation	H/V Flips ( $p = 0.5$ ), Rotation $\pm 15^\circ$ ( $p = 0.7$ )
Data split	70/15/15 (Train/Val/Test on BUSI & HAM), patient-wise stratified (HAM); official test split, 85/15 Train/Val (BRISC)

## D. Gate Training: Derivation and Justification

**Difficulty-aware target derivation.** The soft-IoU between predicted mask and ground truth is computed differentially:

$$\text{IoU}_i = \frac{\sum_p \hat{y}_{ip} y_{ip}}{\sum_p \hat{y}_{ip} + \sum_p y_{ip} - \sum_p \hat{y}_{ip} y_{ip} + \varepsilon}. \quad (17)$$

This is min-max normalised within the mini-batch:

$$\tilde{t}_i = \frac{\text{IoU}_i - \min_j \text{IoU}_j}{\max_j \text{IoU}_j - \min_j \text{IoU}_j + \varepsilon}, \quad (18)$$

and inverted to assign target 1 to the hardest sample:

$$t_i^{\text{seg}} = 1 - \tilde{t}_i. \quad (19)$$

For classification, the maximum predicted class probability  $c_i = \max_k p_{ik}$  is analogously normalised and inverted:

$$t_i^{\text{clf}} = 1 - \frac{c_i - \min_j c_j}{\max_j c_j - \min_j c_j + \varepsilon}. \quad (20)$$

**Gate regularization loss.** The gate is trained by minimizing BCE between each target and its gate weight, summed over both tasks and averaged over all four UPA levels:

$$\mathcal{L}_{\text{gate}} = \frac{\lambda_{\text{gate}}}{4} \sum_{\ell=1}^4 (\text{BCE}(t^{\text{seg}}, w_{\text{seg}}^\ell) + \text{BCE}(t^{\text{clf}}, w_{\text{clf}}^\ell)). \quad (21)$$

**Convergence analysis.** The BCE loss has a global minimum at  $w_i = t_i$ . Since  $t_i^{\text{seg}}$  is computed from  $\text{sg}[\hat{y}]$  (stop-gradient), the gate loss does not back-propagate through the segmentation predictions, preventing the gate from gaming the soft-IoU score rather than tracking genuine sample difficulty. The two-stage protocol further ensures the gate is fine-tuned after the main network has converged, so targets are computed from a stable predictor.

## E. UPA Uncertainty Analysis

This section provides the complete per-dataset signal-quality tables and figures for the Uncertainty Proxy Attention (UPA) analysis. For BUSI, the single-level ROC curves, precision-recall curves, and TIM enhancement figure appear in the main paper; the remaining analysis is reported here. For BRISC and HAM10000 all figures are included. All metrics are computed on the test set used for main-paper segmentation and classification evaluation.

**MC Dropout configuration.** Dropout (rate 0.3, classification head only) is applied at inference; uncertainty estimates average 30 stochastic forward passes without post-hoc calibration.

### E.1. Cross-Dataset Summary

Table A2 summarises segmentation-failure detection across all three datasets using the AUC-weighted combined gate signal and the best single-level signal per dataset. Best-level results report the strongest signal at the strongest decoder level; since the same level ranks highest consistently across all three random seeds, these results characterize a structural property of the architecture and are not sensitive to the specific test partition. The AUC-weighted combination assigns weights from per-level AUC-ROC scores and should be interpreted as a diagnostic summary of signal quality rather than a tuned deployment protocol. We further define the gate differential  $\delta_\ell = w_{\text{clf}} - w_{\text{seg}}$ , which quantifies the relative task preference of the gate at level  $\ell$ . Negative values indicate the gate allocates more enhancement budget to segmentation, empirically correlating with hard segmentation samples (Figs. A2 A15 A8).

### E.2. BUSI - Breast Ultrasound

**Signal quality.** Table A3 reports segmentation-error detection AUC-ROC across all four decoder levels and all UPA

Table A2. Segmentation-failure detection AUC-ROC and AUPRC. *UPA combined*: AUC-weighted fusion of  $-\delta$  across  $D_1$ – $D_4$ . *UPA best*: strongest signal at the strongest decoder level per dataset. Random AUPRC equals the per-dataset segmentation-error rate.

Dataset	MC (30×)		UPA combined		UPA best level	
	AUC	AP	AUC	AP	AUC (signal, level)	AP
BUSI	0.751	0.431	<b>0.807</b>	<b>0.610</b>	<b>0.824</b> ( $w_{\text{seg}}, D_2$ )	<b>0.602</b>
BRISC	0.702	0.238	<b>0.806</b>	<b>0.332</b>	<b>0.852</b> ( $-\delta, D_3$ )	<b>0.470</b>
HAM10000	0.891	0.151	<b>0.927</b>	0.073	<b>0.934</b> ( $w_{\text{seg}}, D_3$ )	0.079

HAM10000 AUPRC is uninformative: seg-error rate = 0.010; random baseline  $\approx$  0.010. All HAM10000 uncertainty claims therefore rest on AUC-ROC only.

signals. Table A4 reports classification-error detection. Entries marked \* beat the MC Dropout reference.

Table A3. BUSI Seg-error AUC-ROC. MC ref = 0.751. \* = beats MC. Bold = best per level.

Signal	D1 (14×14)	D2 (28×28)	D3 (56×56)	D4 (112×112)
$-\delta$	0.674	<b>0.797*</b>	0.461	0.687
$-\text{align}$	0.236	0.803*	0.728	0.206
seg_energy	0.331	0.267	0.285	0.330
$w_{\text{seg}}$	0.767*	<b>0.824*</b>	0.682	0.785*

MC Dropout 0.751 (30 passes)

Table A4. BUSI Clf-error AUC-ROC. MC ref = 0.728; 1-conf = 0.834. \* = beats MC.

Signal	D1	D2	D3	D4
$-\delta$	0.435	0.523	0.306	0.580
clf_energy	0.286	0.223	0.244	0.351
$w_{\text{clf}}$	0.768*	0.716	0.725	<b>0.850*</b>
$-\text{align}$	0.402	0.754*	0.511	0.201

MC Dropout 0.728  
1-conf 0.834

**Combined gate output.** Table A5 shows the combined gate output and MC Dropout for segmentation failure detection.

Table A5. BUSI Combined UPA gate vs MC Dropout, seg error.

Method	AUC	AUPRC	ECE
MC Dropout (ref.)	0.751	0.431	0.102
UPA $-\delta$ mean D1–D4	0.772	0.554	0.363
UPA $-\delta$ AUC-weighted	<b>0.807</b>	<b>0.610</b>	0.237
UPA $-\delta$ best D2	0.797	0.573	0.172

**Gate interpretability.** Table A6 reports Spearman  $\rho$  between UPA signals and MC Dropout uncertainty.  $\checkmark = |\rho| > 0.3, p < 0.05$ .

Table A6. BUSI Spearman  $\rho$  vs MC Dropout.

Pair	D1	D2	D3	D4
seg_energy vs MC seg	$\checkmark -0.586$	$\checkmark -0.653$	$\checkmark -0.689$	$\checkmark -0.661$
$\delta$ vs MC seg	+0.203	-0.055	$\checkmark +0.601$	$\checkmark +0.435$
align vs MC MI	-0.014	-0.269	+0.097	+0.154
$\delta$ vs MC ent	+0.262	+0.091	$\checkmark +0.334$	+0.147

Note: seg\_energy is anti-correlated with MC seg on BUSI (negative  $\rho$ ), contrast to BRISC. See E.5.

**Gate  $\delta$  wrong vs correct.** D1:  $t = -0.52, p = 0.602$ ; D4:  $t = -0.55, p = 0.585$ . Neither is significant; this result is not claimed as supportive evidence.

Figure A1 shows scale sensitivity across decoder levels. Figure A2 shows gate  $\delta$  versus foreground IoU and classifier confidence. Figure A3 shows the full signal-quality heatmap. Figure A4 shows the combined gate ROC.

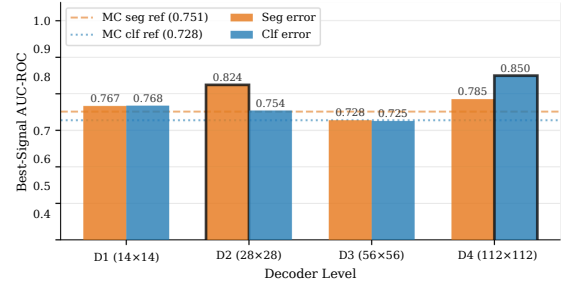


Figure A1. BUSI Scale sensitivity. Each bar shows the best-signal AUC-ROC at that decoder level. Bold border = best level. Dashed/dotted lines = MC Dropout reference.

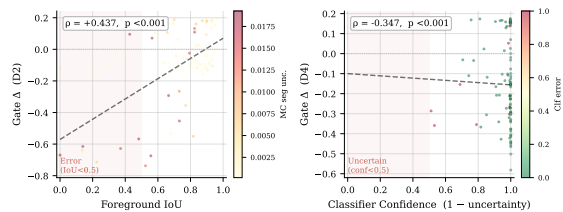


Figure A2. BUSI Gate  $\delta$  interpretability. *Left*:  $\delta$  vs foreground IoU at D2 ( $\rho = +0.437, p < 0.001$ ); colour = MC seg uncertainty. *Right*:  $\delta$  vs classifier confidence at D4 ( $\rho = -0.347, p < 0.001$ ); colour = clf error.

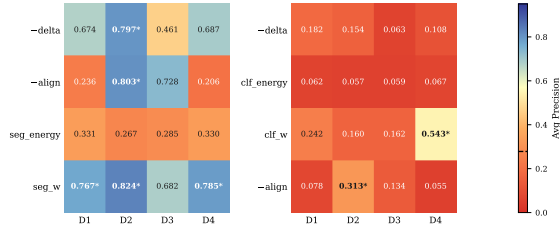


Figure A3. BUSI Signal-quality heatmap. *Left*: seg-error AUC-ROC per signal  $\times$  level. *Right*: clf-error Avg Precision. \* = beats MC Dropout; dashed line on colorbar = MC reference.

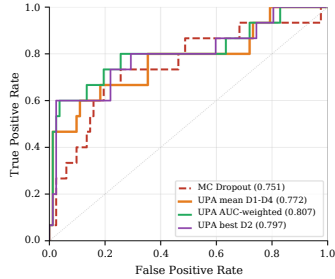


Figure A4. BUSI Combined gate ROC. AUC-weighted fusion (green) achieves 0.807 vs MC Dropout 0.751.

### E.3. BRISC - Brain MRI

Table A7. BRISC Seg-error AUC-ROC. MC ref = 0.702. \* = beats MC.

Signal	D1	D2	D3	D4
- $\delta$	0.413	0.556	<b>0.852*</b>	0.515
-align	0.579	0.512	0.823*	0.467
seg_energy	0.603	0.566	0.509	0.445
w_seg	0.282	0.482	0.834*	0.518
MC Dropout	0.702			

Table A8. BRISC Clf-error AUC-ROC. MC ref = 0.397 (anti-correlated entropy; 1-conf = 0.920). \* = beats MC.

Signal	D1	D2	D3	D4
- $\delta$	<b>0.753*</b>	0.600*	0.597*	0.683*
clf_energy	0.516*	0.509*	0.518*	0.426*
w_clf	0.509*	0.537*	0.575*	0.395
-align	0.306	0.393	0.607*	0.279
MC Dropout	0.397 (miscalibrated; see note)			
1-conf	0.920			

MC entropy anti-correlated on BRISC; all UPA signals beat MC trivially. Do not interpret as UPA clf victory over a valid baseline.

Table A9. BRISC Combined UPA gate vs MC Dropout, seg error.

Method	AUC	AUPRC	ECE
MC Dropout (ref.)	0.702	0.238	0.091
UPA - $\delta$ mean D1-D4	0.635	0.198	0.281
UPA - $\delta$ AUC-weighted	<b>0.806</b>	<b>0.332</b>	0.395
UPA - $\delta$ best D3	0.852	0.470	0.420

Table A10. BRISC Gate  $\delta$  wrong vs correct clf. Both levels significant.

	$n_{\text{wrong}}$	$\bar{\delta}_{\text{wrong}}$	$n_{\text{correct}}$	$\bar{\delta}_{\text{correct}}$	$t$	$p$
D1	14	-0.309	846	-0.129	-3.29	0.001 $\checkmark$
D4	14	-0.139	846	-0.036	-2.48	0.014 $\checkmark$

Table A11. BRISC Spearman  $\rho$  vs MC Dropout.  $\checkmark = |\rho| > 0.3$ ,  $p < 0.05$ .

Pair	D1	D2	D3	D4
seg_energy vs MC seg	+0.252	+0.212	+0.258	-0.094
$\delta$ vs MC seg	-0.114	+0.055	-0.013	$\checkmark$ +0.370
align vs MC MI	+0.116	+0.186	-0.090	+0.085
$\delta$ vs MC ent	-0.210	+0.031	+0.029	+0.160

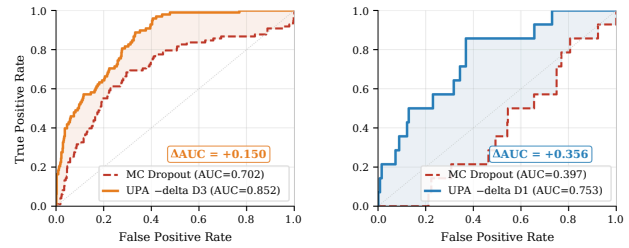


Figure A5. BRISC Single-level ROC. *Left*: seg-error, UPA - $\delta$  D3 (AUC=0.852) vs MC (0.702),  $\Delta\text{AUC} = +0.150$ . *Right*: clf-error, UPA - $\delta$  D1 (AUC=0.753) vs MC (0.397); note MC entropy is anti-correlated on BRISC.

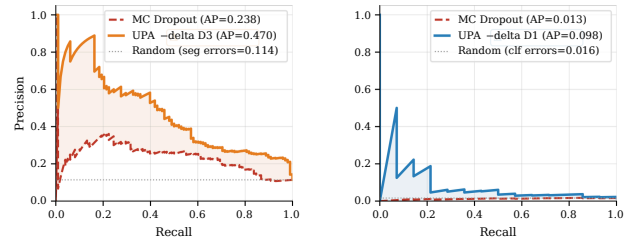


Figure A6. BRISC Precision-recall curves. *Left*: seg-error, UPA AP=0.470 vs MC AP=0.238. *Right*: clf-error shown for completeness; MC baseline is unreliable (random clf-error rate = 0.016).

### E.4. HAM10000 - Dermoscopy

This subsection presents the comprehensive failure detection tables, scale-sensitivity charts, and gate interpretability

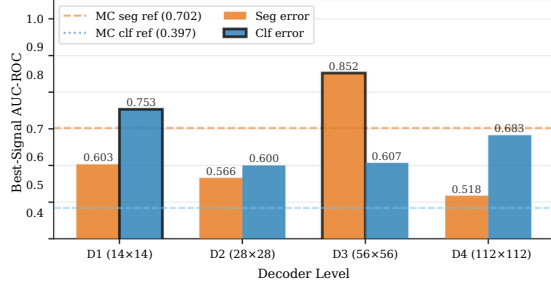


Figure A7. BRISC Scale sensitivity. D3 is the best level for seg. Clf bars all exceed the miscalibrated MC reference (0.397).

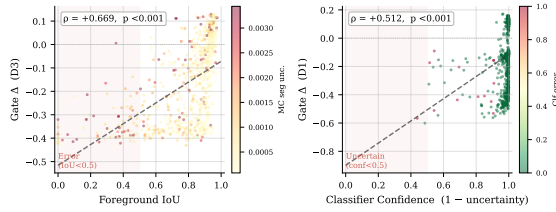


Figure A8. BRISC Gate  $\delta$  interpretability. *Left*:  $\rho(\delta, \text{IoU}) = +0.669$  at D3 ( $p < 0.001$ ). *Right*:  $\rho(\delta, \text{conf}) = +0.512$  at D1 ( $p < 0.001$ ).

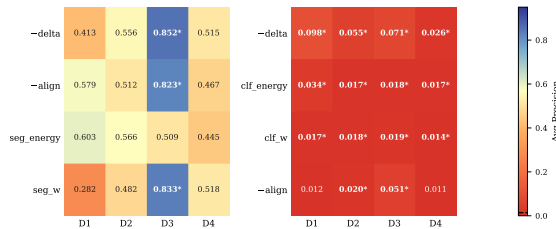


Figure A9. BRISC Signal-quality heatmap. Seg (left): D3 is strongly informative; D1/D2/D4 are near chance. Clf (right): all signals near random baseline given tiny clf error rate ( $\approx 1.6\%$ ).

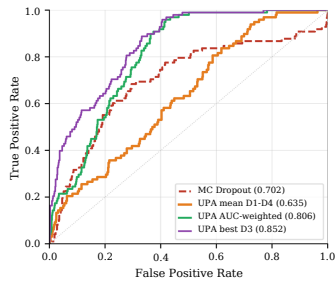


Figure A10. BRISC Combined gate ROC. AUC-weighted fusion achieves 0.806; simple mean (0.635) falls below MC because D1/D2/D4 are below chance and drag the average down. This motivates the AUC-weighted combination strategy.

figures for the HAM10000 dermoscopy dataset.

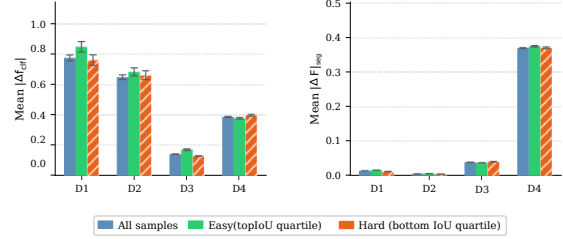


Figure A11. BRISC TIM enhancement magnitudes. *Left* (Seg $\rightarrow$ Clf): hard samples show comparable or larger enhancement than easy samples at D1–D2 but converge at D4. *Right* (Clf $\rightarrow$ Seg): magnitudes are small at D1–D2, growing at D3–D4; hard/easy difference is negligible.

Table A12. HAM Seg-error AUC-ROC. MC ref = 0.891. \* = beats MC.

Signal	D1	D2	D3	D4
$-\delta$	0.814	0.916*	0.885	0.922*
$-\text{align}$	0.898*	0.081	0.062	0.924*
seg_energy	0.333	0.276	0.143	0.415
$w_{\text{seg}}$	0.901*	0.918*	<b>0.934*</b>	0.926*
MC Dropout	0.891			

Table A13. HAM Clf-error AUC-ROC. MC ref = 0.575; 1-conf = 0.834. \* = beats MC.

Signal	D1	D2	D3	D4
$-\delta$	0.435	0.597*	0.631*	0.736*
clf_energy	0.260	0.589*	0.514	0.302
$w_{\text{clf}}$	<b>0.766*</b>	0.513	0.609*	0.518
$-\text{align}$	0.707*	0.413	0.376	0.640*
MC Dropout	0.575			
1-conf	0.834			

Table A14. HAM Combined UPA gate vs MC Dropout, seg error. Note: HAM AUPRC is unreliable (seg error rate = 1.0%).

Method	AUC	AUPRC $^\dagger$	ECE
MC Dropout (ref.)	0.891	0.151	0.072
UPA $-\delta$ mean D1–D4	0.925	0.071	0.214
UPA $-\delta$ AUC-weighted	<b>0.927</b>	0.073	0.212
UPA $-\delta$ best D4	0.922	0.080	0.282

$^\dagger$  AUPRC not meaningful: random baseline  $\approx 0.010$  = error rate.

## E.5. Discussion of Cross-Dataset Anomalies

### Negative Spearman correlations on BUSI and HAM.

On BUSI, seg\_energy is negatively correlated with MC seg uncertainty across all decoder levels (Table A6). On HAM,  $\delta$  and seg\_energy show mixed-sign correlations at D2–D3 (Table A16). Both anomalies occur on datasets where the model achieves high predictive accuracy (BUSI Clf Acc = 93.16%; HAM Clf Acc = 87.8%). Thus in high-accuracy regimes,

Table A15. HAM Gate  $\delta$  wrong vs correct clf. D4 is strongly significant; D1 is not.

	$n_{\text{wrong}}$	$\bar{\delta}_{\text{wrong}}$	$n_{\text{correct}}$	$\bar{\delta}_{\text{correct}}$	$t$	$p$
D1	331	-0.025	1160	-0.016	-1.75	0.080
D4	331	+0.223	1160	+0.259	-9.13	<0.001 ✓

At D4, wrong-class samples carry *lower*  $\delta$  than correct ones, consistent with greater seg-clf task tension on hard samples.

Table A16. HAM Spearman  $\rho$  vs MC Dropout. ✓ =  $|\rho| > 0.3$ ,  $p < 0.05$ . Note mixed-sign correlations at D2–D3 reflect inverted signal regime at near-zero error rates.

Pair	D1	D2	D3	D4
seg_energy vs MC seg	✓+0.388	-0.112	✓-0.440	-0.253
$\delta$ vs MC seg	✓-0.387	✓-0.663	✓-0.540	-0.103
align vs MC MI	✓-0.522	+0.287	✓+0.323	✓-0.387
$\delta$ vs MC ent	-0.141	✓-0.312	✓-0.313	-0.252

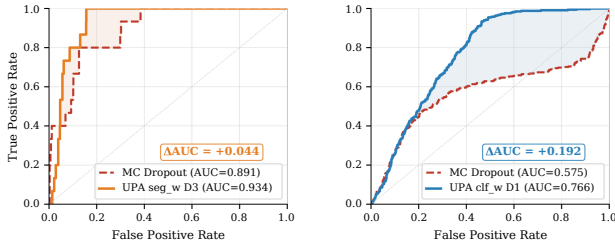


Figure A12. HAM Single-level ROC. *Left*: seg-error,  $w_{\text{seg}}$  D3 (AUC=0.934) vs MC (0.891),  $\Delta\text{AUC} = +0.044$ . *Right*: clf-error,  $w_{\text{clf}}$  D1 (AUC=0.766) vs MC (0.575),  $\Delta\text{AUC} = +0.192$ .

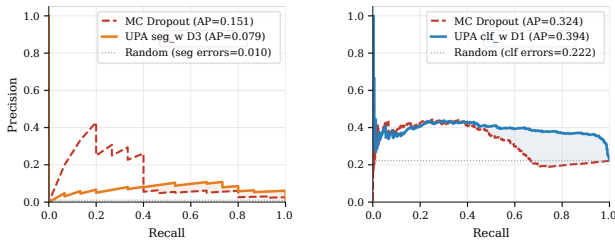


Figure A13. HAM Precision-recall curves. *Left*: seg-error PR; UPA AP = 0.079 vs MC AP = 0.151; both near random (0.10) AUPRC is not a meaningful metric at 1% error prevalence. *Right*: clf-error PR; UPA  $w_{\text{clf}}$  D1 AP = 0.394 vs MC AP = 0.324.

MC Dropout variance is dominated by the network’s weight uncertainty on easy samples (which are numerous), while UPA gate signals are tuned toward hard-sample difficulty. The resulting inversion in rank-order correlation does not contradict the main detection-AUC results:  $w_{\text{seg}}$  still correctly ranks hard segmentation samples above easy ones (positive Spearman  $\rho$  with IoU, all datasets).

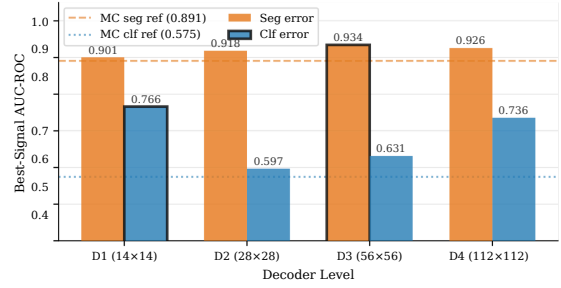


Figure A14. HAM Scale sensitivity.  $w_{\text{seg}}$  consistently exceeds MC reference (0.891) at all four decoder levels. Clf signal ( $w_{\text{clf}}$ ) peaks at D1.

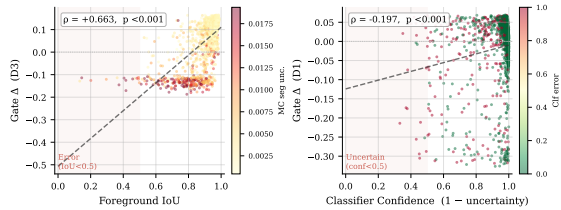


Figure A15. HAM Gate  $\delta$  interpretability. *Left*:  $\rho(\delta, \text{IoU}) = +0.663$  at D3 ( $p < 0.001$ ), consistent with BUSI and BRISC. *Right*:  $\rho(\delta, \text{conf}) = -0.197$  at D1 ( $p < 0.001$ ); significant but weaker than seg panel, reflecting limited clf discriminability at this class-imbalance level.

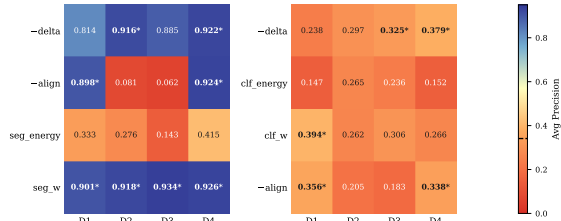


Figure A16. HAM Signal-quality heatmap.  $w_{\text{seg}}$  (bottom row, left panel) shows strong, consistent signal across all decoder levels, the only dataset where D4 also beats MC comfortably.

**HAM AUPRC.** The segmentation error rate on HAM is approximately 1% (random baseline AUPRC  $\approx 0.010$ ). AUPRC at this prevalence is dominated by chance precision at high recall thresholds and is not a reliable metric. All HAM uncertainty claims are therefore based exclusively on AUC-ROC.

**BRISC MC Dropout clf failure.** MC Dropout entropy is anti-correlated with classification errors on BRISC (AUC = 0.397, below chance). This reflects a known failure mode of entropy-based MC Dropout when the model is overconfident on the wrong class. The 1-confidence baseline (AUC = 0.920) succeeds because the model’s softmax output

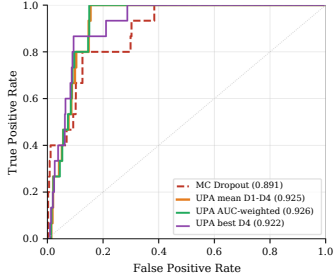


Figure A17. HAM Combined gate ROC. Both mean and AUC-weighted combinations exceed MC (0.891). The simple mean performs comparably to the weighted version, reflecting that  $-\delta$  is informative at all four levels on HAM.

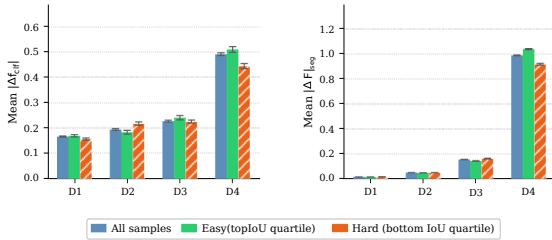


Figure A18. HAM TIM enhancement magnitudes. *Left* (Seg→Clf): hard samples (orange) receive lower Seg→Clf enhancement than easy samples at all levels, unlike BUSI and BRISC, suggesting TIM adaptive routing is modality dependent. *Right* (Clf→Seg): easy samples receive marginally larger enhancement; hard/easy gap is small.

is well-calibrated despite the entropy failure. UPA clf signals ( $-\delta$  at D1, AUC = 0.753) partially recover clf uncertainty detection without requiring post-hoc calibration, but do not match 1-conf on this dataset.

## F. Per-Dataset Segmentation Metrics

Table A17 reports segmentation performance on positive-mask test cases for all three datasets. Metrics are computed per-image and averaged; BUSI excludes the Normal class (empty masks) from this computation. HAM10000 reports over all test cases as every image contains a lesion.

Table A17. Segmentation on positive-mask test cases.

Dataset	Dice	IoU	Med. Dice	Prec.	Rec.
BUSI ( $n=97$ )	85.3 ± 0.7	74.5 ± 0.3	90.4	85.5	83.1
BRISC ( $n=860$ )	84.5 ± 0.4	76.7 ± 0.5	92.3	84.2	88.1
HAM ( $n=1503$ )	94.2 ± 0.9	89.8 ± 0.2	96.8	94.9	94.6

## G. Per-Dataset Classification Results

Table A18 reports classification performance on all three test sets. Weighted averages are reported; HAM10000 F1 slightly lower due to class imbalance (the nevus (nv) class constitutes 67% of the test cases).

Table A18. Classification performance on test sets.

Dataset	$n$	Acc.	Prec.	Recall	F1
BUSI	117	93.2 ± 0.8	0.93	0.93	0.93
BRISC	1000	99.1 ± 0.2	0.99	0.99	0.99
HAM	1503	87.8 ± 0.6	0.87	0.88	0.87

## H. Failure Case Analysis

Figure A19 presents a qualitative analysis of representative failure modes across the three imaging modalities. These comparisons illustrate how modality-specific artifacts and ambiguous pathological boundaries drive localized degradation in segmentation fidelity.

## I. Reproducibility Statement

All experiments use three independent random seeds (42, 123, 456) applied to data splitting, weight initialisation, and augmentation ordering. The source code, including pre-processing scripts, model definitions, training pipelines, and evaluation notebooks, will be released under an open-source licence upon publication. Pre-trained weights for the proposed model and all reproduced baselines, the exact train/validation/test splits per seed, and per-seed result logs will be made publicly available. All experiments are reproducible from the provided configuration files using the hardware and software environment documented in Table A1.

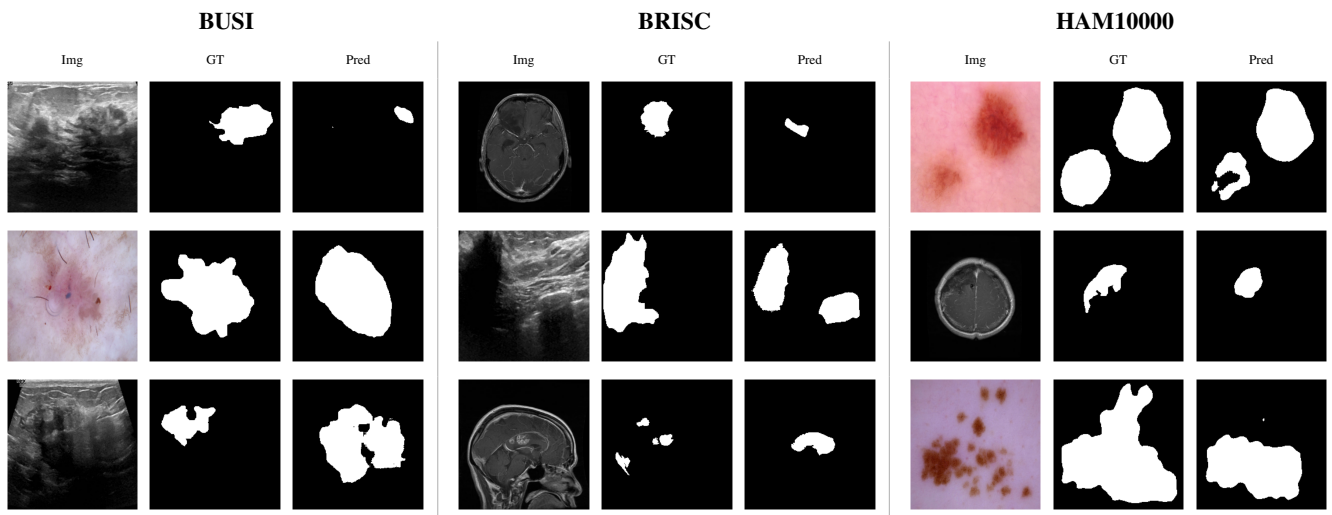


Figure A19. Representative failure cases across all three datasets. Each group shows input image, ground-truth mask, and predicted mask. **BUSI**: acoustic shadows misidentified as lesion boundary in heavily shadowed regions, leading to over-segmentation. **BRISC**: tumour margins obscured by perilesional oedema cause boundary underestimation despite correct localisation. **HAM10000**: lesions with subtle colour gradients and ill-defined margins produce fragmented predictions. In these cases, the UPA uncertainty signals indicate unreliable interaction, consistent with the failure-detection analysis in Sec E.